AGU PUBLICATIONS

JGR

Journal of Geophysical Research: Atmospheres

RESEARCH ARTICLE
10.1002/2015JD024037

Key Points:
- Polar WRF is a useful tool for modeling West Antarctic climate
- Little sensitivity found between 5 and 15 km horizontal resolution
- MYJ boundary layer scheme gives better representation of diurnal cycle in near-surface temperature

Correspondence to:
P. Deb,
prab@bas.ac.uk

Citation:
Deb, P., A. Orr, J. S. Hosking, T. Phillips, J. Turner, D. Bannister, J. O. Pope, and S. Colwell (2016), An assessment of the Polar Weather Research and Forecasting (WRF) model representation of near-surface meteorological variables over West Antarctica, *J. Geophys. Res. Atmos.*, *121*, 1532–1548, doi:10.1002/2015JD024037.

Received 3 AUG 2015
Accepted 15 JAN 2016
Accepted article online 22 JAN 2016
Published online 19 FEB 2016

An assessment of the Polar Weather Research and Forecasting (WRF) model representation of near-surface meteorological variables over West Antarctica

Pranab Deb[1], Andrew Orr[1], J. Scott Hosking[1], Tony Phillips[1], John Turner[1], Daniel Bannister[1], James O. Pope[1], and Steve Colwell[1]

[1]British Antarctic Survey, Cambridge, UK

Abstract Despite the recent significant climatic changes observed over West Antarctica, which include large warming in central West Antarctica and accelerated ice loss, adequate validation of regional simulations of meteorological variables are rare for this region. To address this gap, results from a recent version of the Polar Weather Research and Forecasting model (Polar WRF) covering West Antarctica at a high horizontal resolution of 5 km were validated against near-surface meteorological observations. The model employed physics options that included the Mellor-Yamada-Nakanishi-Niino boundary layer scheme, the WRF Single Moment 5-Class cloud microphysics scheme, the new version of the rapid radiative transfer model for both shortwave and longwave radiation, and the Noah land surface model. Our evaluation finds this model to be a useful tool for realistically capturing the near-surface meteorological conditions. It showed high skill in simulating surface pressure (correlation ≥0.97), good skill for wind speed with better correlation at inland sites (0.7–0.8) compared to coastal sites (0.3–0.6), generally good representation of strong wind events, and good skill for temperature in winter (correlation ≥0.8). The main shortcomings of this configuration of Polar WRF are an occasional failure to properly represent transient cyclones and their influence on coastal winds, an amplified diurnal temperature cycle in summer, and a general tendency to underestimate the wind speed at inland sites in summer. Additional sensitivity studies were performed to quantify the impact of the choice of boundary layer scheme and surface boundary conditions. It is shown that the model is most sensitive to the choice of boundary layer scheme, with the representation of the temperature diurnal cycle in summer significantly improved by selecting the Mellor-Yamada-Janjic boundary layer scheme. By contrast, the model results showed little sensitivity to whether the horizontal resolution was 5 or 15 km.

1. Introduction

Recent observations have highlighted that significant regional climate changes are occurring in West Antarctica. These include an acceleration of ice loss at a current rate of $134 \pm 27\ \mathrm{Gt\,yr^{-1}}$ from West Antarctica [*McMillan et al.*, 2014], as well as annually averaged near-surface warming rates of ~0.5°C per decade (which is many times greater than the global average) detected at Byrd Station in central West Antarctica [*Bromwich et al.*, 2013a]. However, although this suggests that present-day West Antarctic climate change is both amplified and highly significant within the global climate system, West Antarctic wide understanding of the spatial and temporal variability of basic parameters such as air temperature and precipitation is still lacking.

One of the principal reasons for our poor understanding of present-day West Antarctic climate is that with the exception of Byrd Station, there are no long-term weather records necessary for climatological studies [*Bromwich et al.*, 2013a]. The lack of in situ observations is largely due to the hostile and remote environment which characterizes West Antarctica, making such measurements highly challenging. Thus, although parts of the maritime west coast of the Antarctic Peninsula have undergone the largest recorded temperature increase across the Southern Hemisphere [*King et al.*, 2003], the magnitude of the warming and the extent to which this warming extends into West Antarctica are still being debated. In recent years, our understanding of West Antarctic climate has been aided somewhat by satellite measurements and automatic weather station (AWS) data, particularly when such data are used in conjunction with statistical techniques which have allowed the reconstruction of past near-surface temperatures with greatly increased spatial and temporal coverage [e.g., *Steig et al.*, 2009; *O'Donnell et al.*, 2011]. Although such reconstructions broadly agree that West Antarctica has warmed since the 1950s, the lack of consensus of the seasonal and spatial patterns of the warming only serves to highlight the uncertainty of climate change across West Antarctica.

It is clear, therefore, that more work is required to better understand the present-day climate of West Antarctica. Clarification of regional-scale patterns in temperature and precipitation is particularly important, since both of these parameters control ice sheet mass balances via accumulation and ablation. Better understanding of surface mass balance [e.g., *van de Berg et al*., 2006; *Medley et al*., 2014] is urgently required by the ice sheet modeling community to facilitate improved modeling of the mass balance of West Antarctica, which is dominated by dynamic losses from the Amundsen Sea sector [*Pritchard et al*., 2012; *McMillan et al*., 2014]. However, the scarcity of observational data, coarse spatial resolution, and simplified physical parameterization make it difficult for both global reanalysis data sets and global climate models to represent the complex regional scale processes which characterize West Antarctica [e.g., *Condron et al*., 2008; *Turner et al*., 2009; *Uotila et al*., 2009; *Condron and Renfrew*, 2013; *Medley et al*., 2014; *Orr et al*., 2014]. For example, the high spatial variability of West Antarctica's complex orography and coastline can result in significant regional near-surface variations of wind, temperature, and precipitation [e.g., *Parish and Bromwich*, 1998; *Hunt et al*., 2004; *Orr et al*., 2005, 2014; *Owinoh et al*., 2005; *Webster et al*., 2008; *Valkonen et al*., 2010]. Moreover, small mesocyclones (scales of a few hundred kilometers) are particularly prominent in the Amundsen and Bellingshausen Seas during summer and autumn [*Irving et al*., 2010]. These systems, together with their synoptic-scale counterparts [*Simmonds et al*., 2003], constitute the climatological area of low pressure known as the Amundsen Sea Low which is a key factor of West Antarctic regional climatic variability [*Hosking et al*., 2013].

To this end, an appropriate tool to generate fine-scale, dynamically, and physically consistent regional scale fields is by dynamically downscaling the global reanalysis data using high-resolution regional scale atmospheric models [e.g., *Giorgi et al*., 1994]. In this approach the reanalysis data are used to provide time-dependent surface and lateral boundary conditions to drive the regional scale model. Since the reanalysis data describe the dominant large-scale driving forces, such as the Southern Annular Mode [*Thompson and Wallace*, 2001] and El Niño–Southern Oscillation [*Lachlan-Cope and Connolley*, 2006], this approach ensures that the regional scale model results are realistically constrained.

The representation of physical processes such as the planetary boundary layer, surface layer, and clouds are particularly vital for regional simulations of West Antarctica. Previous studies have suggested that models generally struggle to simulate important cloud properties such as cloud phase and cover in the high latitudes, and as a consequence the surface energy budget is also poorly represented [*Fogt and Bromwich*, 2008; *Wilson et al*., 2012; *Bromwich et al*., 2013b; *King et al*., 2015]. The extremely cold temperatures over the icy surface of West Antarctica frequently results in a highly stable boundary layer, characterized by sharp vertical gradients in wind and temperature which models typically fail to reproduce [e.g., *Cuxart et al*., 2006; *Tastula and Vihma*, 2011; *Valkonen et al*., 2014]. Moreover, around West Antarctica the sea ice cover is characterized by small-scale polynyas and leads [e.g., *Arrigo et al*., 2012], which because they are ice free in otherwise ice-covered seas can have a significant impact on the heat and momentum budget of the atmosphere [*Owinoh et al*., 2005; *Tastula et al*., 2012]. Models also find the interaction between surface layer and boundary layer processes in polar regions to be problematic [*Holtslag et al*., 2013; *Sterk et al*., 2013].

In this study we perform high-resolution simulations of West Antarctica for two 1 month periods representative of both winter and summer using a polar-optimized version of the Weather Research and Forecasting model (WRF) [*Skamarock et al*., 2008], which hereafter is referred to as Polar WRF [*Hines and Bromwich*, 2008]. We run the model at a high horizontal resolution (up to 5 km) in order to resolve the above mentioned local scale processes. The simulated temperature, pressure, and wind are compared with observations from four AWSs representative of both coastal and inland locations. In situ observations of precipitation are unfortunately not available. Our aim is to assess the reliability of Polar WRF and also to investigate its sensitivity to changes in the model setup (e.g., the treatment of the boundary layer, surface boundary conditions, and use of spectral nudging in the downscaling). The different model setups will be discussed in detail in the following section. Of the number of Polar WRF validation studies which have been performed in recent years for the Antarctic [e.g., *Valkonen et al*., 2010, 2014; *Tastula and Vihma*, 2011; *Tastula et al*., 2012; *Nigro et al*., 2012a, 2012b; *Bromwich et al*., 2013b; *Steinhoff et al*., 2014; *King et al*., 2015], to our knowledge this is the first to focus on West Antarctica.

We view this study as an important stepping stone toward our goal of using Polar WRF to generate a high-resolution climatology of key meteorological parameters of West Antarctica, enabling identification of

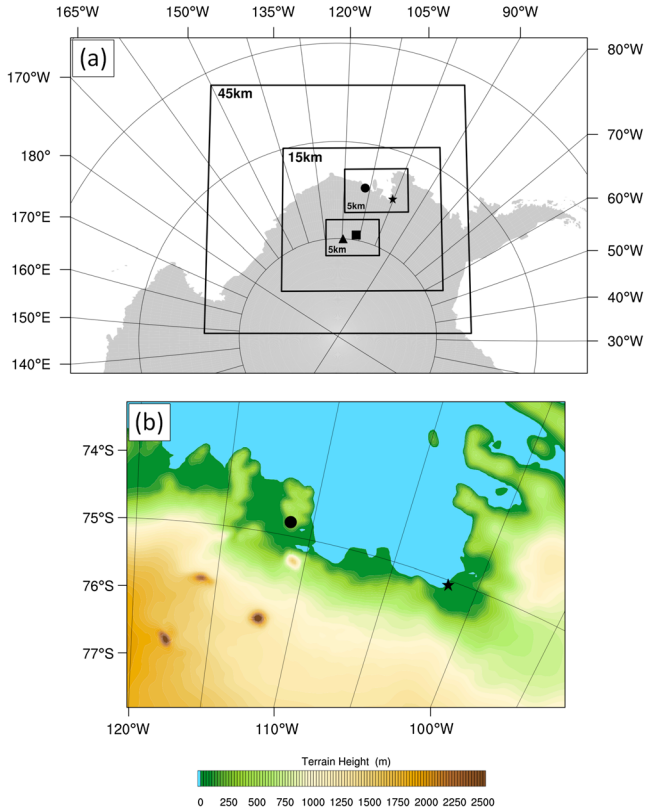

Figure 1. (a) Map showing the location of the Polar WRF domains at horizontal resolutions of 45, 15, and 5 km. Also shown are the locations of the two coastal AWS stations at Bear Peninsula (denoted by a circle) and Evans Knoll (denoted by a star) and the two inland AWS stations at Kominko Slade (denoted by a square) and Byrd (denoted by a triangle). (b) Enlarged view of the 5 km coastal domain showing the model orography based on the GTOPO30 data set (m, shaded), as well as the location of two coastal AWS stations.

the mechanisms responsible for recent climate change. Section 2 describes the model, the in situ observations used and the experiments performed. Section 3 is split into two parts: first, detailing the performance of the model for both inland and coastal stations and, second, describing the results of the sensitivity tests. Section 4 will discuss the results.

2. Model Description and Experimental Design

2.1. Model Description

This work uses the version 3.5.1 of Polar WRF. Polar WRF model is a state-of-the-art limited-area mesoscale modeling system [*Skamarock et al.*, 2008]. It solves a fully compressible nonhydrostatic system of equations on an Arakawa C-grid in the horizontal. A terrain-following coordinate system is employed in the vertical. The time-split integration uses a third-order Runge-Kutta scheme. Polar WRF includes important modifications in order to better represent the key regional physical processes which are important for the polar regions, namely, an enhanced treatment of the snowpack, sea-ice, and cloud radiative processes [*Hines and Bromwich*, 2008]. The physics options employed throughout this study include the new version of the rapid radiative transfer model [*Iacono et al.*, 2008] for general circulation models (RRTMG) for both shortwave and longwave radiations, the WRF Single Moment 5-Class (WSM5) cloud microphysics scheme [*Hong et al.*, 2004], and the Noah land surface model [*Chen and Dudhia*, 2001] with modifications by *Hines and Bromwich* [2008]. These physics options were chosen after consideration of previous evaluation studies, particularly *Bromwich et al.* [2013b]. For the boundary layer we initially use the more recent Mellor-Yamada-Nakanishi-Niino (MYNN) turbulent kinetic energy (TKE) scheme [*Nakanishi and Niino*, 2006], run in conjunction with the MYNN surface layer scheme (which was also considered by *Bromwich et al.* [2013b]). Note, two additional boundary layer schemes will also be evaluated, as described in section 2.4.

Our setup uses a number of one-way nested domains with horizontal grid spacing of 45, 15, and 5 km. The locations of the domains are shown in Figure 1a. The outermost or the largest domain uses 45 km resolution and comprises 68×64 grid points covering the West Antarctic Ice Sheet and a large ocean area including the Amundsen and Bellingshausen Seas (so as to resolve the important forcing from mesocyclones, as discussed above). Nested within this is a smaller-sized domain which uses 15 km resolution and comprises 121×109 grid points encompassing a major portion of the ice sheet and part of the Amundsen Sea. Nested within the 15 km domain are two 5 km domains representative of the so-called "coastal" and "inland" regions. The coastal domain comprises 145×100 grid points and encompasses one of the main regions where the ice sheet drains into the Amundsen Sea via outlet glaciers such as Pine Island Glacier and Thwaites Glacier. The inland domain comprises 121×82 grid points and covers a flat region of central West Antarctica which encompasses Byrd Station. Time steps of 180, 60, and 20 s were selected (based on initial sensitivity studies as

Table 1. Locations and Comparison of Actual and Modeled Surface Elevations of the Four AWSs Used in This Study[a]

		Surface Elevation (m)		
			Polar WRF (5 km Resolution Domain)	
Station Name	Location	Actual	Based On GTOPO30	Based On BedMap2
Kominko Slade	112.106°W, 79.466°S	1801	1786.9	1792.9
Byrd	119.404°W, 80.007°S	1530	1520.1	1536.8
Bear Peninsula	111.885°W, 74.546°S	312	303.0	223.1
Evans Knoll	100.404°W, 74.85°S	188	95.8	78.6

[a]The modeled surface elevations are from the Polar WRF domains at 5 km horizontal resolution, based on both GTOPO30 and Bedmap2 orography data sets.

a compromise between minimizing run time and maintaining model stability) for the 45, 15, and 5 km nests, respectively. All the model domains employ 30 vertical levels between the surface and the model top at 50 hPa.

2.2. Model Boundary Conditions

ERA-Interim reanalysis data [*Dee et al*., 2011] are used to initialize the model and to provide forcing of its lateral and surface boundary conditions, updated every 6 h. ERA-Interim has a spatial resolution of N128 (equivalent to a resolution of ~0.7°) and was selected, as *Bracegirdle and Marshall* [2012] demonstrated that it gave, compared to other major reanalysis data sets, the best representation of Antarctica's large-scale circulation. Land-type and topography information for the model was obtained from the default United States Geological Survey 24-category land use data and global 30″ elevation data (GTOPO30), respectively. Figure 1b highlights the complex nature of the coastal terrain.

2.3. Observational Data

The four AWSs used in this study are maintained by the University of Wisconsin. Two of the four sites, referred to as Bear Peninsula and Evans Knoll, are situated within the coastal domain of the model. The remaining two sites, referred to as Kominko Slade and Byrd, are situated within the inland domain. Table 1 gives the latitude and longitude of their locations. Figure 1a shows their location within the inland and coastal domains. The AWSs measure air temperature, wind speed, and direction at a nominal height of 3 m above the surface at a temporal interval of 3 h (i.e., values each day at 0000, 0300, 0600 … 1800, 2100 UTC). Surface pressure is measured near the foot of the mast. Details of the data acquisition techniques and quality control measures adopted by the AWS program can be found at http://amrc.ssec.wisc.edu/aws/.

Table 1 compares the actual surface elevation at each site with the corresponding Polar WRF elevation from the nearest grid point (at 5 km resolution, based on the default GTOPO30 data set). Given the homogeneity of the surface of central West Antarctica, as expected, the actual and model surface elevations are in relatively good agreement for the two inland sites, i.e., within ~10 m of each other. By contrast, for the coastal site of Evans Knoll the actual surface elevation is ~93 m higher than the model surface elevation. Such a considerable disagreement is suggestive that the 5 km spatial resolution of the model is unable to adequately represent the significant surface heterogeneity which characterizes coastal West Antarctica. However, an alternative explanation that the actual elevation measurement is in error cannot be ruled out. The remaining coastal site at Bear Peninsula has a much smaller difference in surface elevation of ~10 m. Note that the actual surface elevation at Bear Peninsula of 312 m was confirmed by an independent measurement using a Global Positioning System unit as a part of the Polar Earth Observing Network.

In addition, infrared composite satellite images (derived from geostationary and polar orbiting satellites) archived by the University of Wisconsin are used to identify large-scale cloud features associated with cyclones.

2.4. Methodology

The Polar WRF model described above (hereafter labeled as "Run A") was run continuously for one summer (January) and one winter (July) month in 2013. In each of our experiments, the model runs started at 0000 UTC on the first day of the month and ended at 1800 UTC on the 30th day of the month. Model fields of surface pressure, grid-relative zonal and meridional wind components at 10 m, and 2 m temperature from

Table 2. Comparison of Monthly Mean 2 m Temperature and Surface Pressure for January (Jan) and July (Jul) 2013 at the Kominko Slade and Bear Peninsula Sites Versus Their Climatological (1979–2015) Monthly Mean ± One Standard Deviation, Computed Using ERA-Interim Data

Station Name	Variables	Jan 2013(Mean)	Jan 1979–2015(Mean ± SD)	Jul 2013(Mean)	Jul 1979–2015 Jul(Mean ± SD)
Kominko Slade	2 m temperature (K)	259.9	257.92 ± 3.33	235.13	238.38 ± 8.31
	Surface pressure (hPa)	791.4	789.46 ± 5.84	773.63	777.58 ± 11.67
Bear Peninsula	2 m temperature (K)	272.46	271.72 ± 1.39	253.28	255.36 ± 7.49
	Surface pressure (hPa)	986.55	983.15 ± 7.92	974.65	979.56 ± 15.75

the 5, 15, and 45 km gridded domains were archived for the duration of the runs at hourly intervals. These were subsequently used to create a time series of surface pressure, 10 m wind speed and direction (derived from the grid-relative wind components) and 2 m temperature at each of the AWS sites for each of the domains, with the model grid point nearest to the location of an AWS chosen as representative of the site. Each of the hourly time series were subsampled to create a monthly 3-hourly time series which coincides with the measurements described in section 2.3. To account for the differences in surface elevation between the model points and AWS sites, the model temperature lapse rate is used to adjust the model 2 m temperature to a value corresponding to the actual elevation. Likewise, the model surface pressure is adjusted to a value corresponding to the actual elevation, using the hypsometric equation. Additionally, the measured wind speed at 3 m is adjusted to a value corresponding to a height of 10 m, using the logarithmic wind profile. The model output was subsequently validated by comparing a monthly 3-hourly model time series with its equivalent measured time series. A statistical measure of the model performance is also employed, based on correlation, mean bias, and root-mean-square error (RMSE), all computed against the adjusted AWS observations [*Bromwich et al*., 2013b].

To show that these months were broadly representative of conditions over West Antarctica, Table 2 uses ERA-Interim data to compare the mean 2 m temperature and surface pressure during January 2013 and July 2013 at an inland station (Kominko Slade) and a coastal station (Bear Peninsula) against the climatological (1979–2015) mean. At each of the sites, both surface pressure and 2 m temperature were higher than average in January 2013, but within one standard deviation of the climatological monthly mean. In July 2013, both surface pressure and 2 m temperature were lower than average, but again within one standard deviation of the climatological monthly mean. Note, the conditions for January and July 2013 were also within one standard deviation of their associated climatological summer (December–February) and winter (June–August) values (not shown).

In addition to this, five sensitivity experiments were also performed, which are listed in Table 3. First, an experiment labeled "Run B" is exactly the same as Run A except that the sea ice fraction and sea surface temperature (SST) data (from ERA-Interim reanalysis) used to force the surface boundary conditions are replaced by high-resolution data (from satellite) which is updated daily. The sea ice data are based on the 25 km resolution Bootstrap data set [*Comiso*, 2000], while the SST data are based on the 0.25° Advanced Very High Resolution Radiometer (AVHRR) data set [*Casey et al*., 2010]. This experiment is designed to represent as realistically as possible the extensive distribution of sea ice in the Amundsen and Bellingshausen Seas (particularly in July). Second, an experiment labeled "Run C" is exactly the same as Run B except the data set used to derive the topography information is based on the ~1 km resolution state-of-the-art digital elevation model Bedmap2 [*Fretwell et al*., 2013]. This experiment is designed to test whether such detailed modeling of near-surface variables in complex coastal regions is sensitive to the representation of topography. For example, Table 1 shows that although the model surface elevations of the two inland stations (Kominko Slade and Byrd) are broadly insensitive to the choice of orography data set, the coastal station of Bear Peninsula shows

Table 3. Label and Description of the Basic (Run A) and Additional Sensitivity Runs (Runs B, C, D, A1, and A2)

Label	Description
Run A	Basic run
Run B	Run A + high-resolution Bootstrap sea ice data + high-resolution AVHRR SST data
Run C	Run B + orography based on Bedmap2 data set
Run D	Run A + spectral nudging
Run A1	Run A + Mellor-Yamada-Janjic (MYJ) boundary layer scheme
Run A2	Run A + Yonsei University (YSU) boundary layer scheme

considerable differences. It should however be noted that the surface elevations for the coastal stations derived from the Bedmap2 data are further away from the actual elevations than the GTOPO30 data. Another experiment was conducted to assess the sensitivity to the use of spectral nudging in the downscaling. This experiment is labeled "Run D" and is exactly the same as Run A except that spectral nudging is applied within the interior of the modeling domain. In spectral nudging, the nudging term comprises only selected wave numbers represented by the driving fields (i.e., the large-scale features), which reduces large-scale drift from the driving fields while still allowing the development of appropriate small-scale features [*von Storch et al*., 2000]. The study by *Liu et al*. [2012] suggested that with the appropriate choice of wave numbers spectral nudging outperforms grid nudging. Here horizontal winds, temperature, specific humidity, and geopotential height are nudged at all vertical levels above the first 10 model levels (i.e., from approximately 1.5 km in altitude to the model top) with a nudging weight of $3 \times 10^{-4}\,s^{-1}$. Wave numbers 1–5 for the 45 km domain, 1–3 for the 15 km domain, and 1 for the 5 km domain are nudged.

Two further experiments were conducted to assess the sensitivity to the boundary layer scheme. An experiment labeled "Run A1" is exactly the same as Run A except that the MYNN boundary layer scheme is replaced by Mellor-Yamada-Janjic (MYJ) boundary layer scheme (in conjunction with the Janjic-Eta Monin Obukhov surface layer scheme) [*Janjić*, 2002]. The MYJ scheme is the default choice for the current configuration of the Antarctic Mesoscale Prediction System [*Powers et al*., 2012]. MYNN and MYJ are both level 2.5 closure TKE-based schemes (although MYNN can also be run at 3.0 level closure). The main difference between them arises from their formulation of mixing length scales, which are tuned to different data sets: MYJ is tuned to observations while MYNN is tuned to large-eddy simulations [*Janjić*, 2002; *Nakanishi and Niino*, 2006]. Lastly, an experiment labeled Run A2 is exactly the same as Run A except that the MYNN scheme is replaced by the Yonsei University (YSU) boundary layer scheme (in conjunction with the Monin Obukhov surface layer scheme) [*Hong*, 2010; *Hong et al*., 2006]. The YSU scheme is a first-order nonlocal scheme containing a counter-gradient term in the eddy-diffusion equation and an explicit treatment of entrainment in the turbulent flux equation. Previous validation studies show that model performance over the polar regions is sensitive to the choice of boundary layer scheme [*Hines and Bromwich*, 2008; *Bromwich et al*., 2009, 2013b; *Tastula and Vihma*, 2011; *Tastula et al*., 2012].

Finally, the infrared cloud images are used to confirm that the large-scale features associated with cyclones are well represented by the ERA-Interim data set (which is subsequently compared to Polar WRF output).

3. Evaluation of Polar WRF Simulations

Comparison of the Run A Polar WRF simulations against the observational data from the inland (Kominko Slade and Byrd) and coastal (Bear Peninsula and Evans Knoll) stations is presented in sections 3.1 and 3.2, respectively. The comparison will predominately focus on the results from the corresponding inland and coastal domains at a horizontal resolution of 5 km. Section 3.3 assesses the impacts of the sensitivity experiments described in Table 3.

3.1. Inland Stations

Figure 2 compares the monthly 3-hourly time series of observations at Kominko Slade during January against the corresponding Polar WRF output at a horizontal resolution of 5 km. The temporal variability of surface pressure is closely captured by the model, suggesting that the effects of synoptic weather systems [*Nicolas and Bromwich*, 2011] over the interior of the study domain are well represented. However, in terms of amplitude the model shows on a number of occasions positive (negative) biases of a few hPa when the pressure is at a minimum (maximum), resulting in a flattening of the pressure variation relative to reality. The temporal variability of 10 m wind speed is also captured well by the model, although there is a general tendency to underestimate the peak wind speed by around 2 to 4 $m\,s^{-1}$ (a notable exception to this is on the 23rd when the peak wind speed of 14 $m\,s^{-1}$ is accurately simulated). Moreover, the model successfully captures the rapid strengthening of wind, e.g., on 5, 22, and 26 January which occurs synchronously with a reduction in surface pressure, i.e., suggestive of synoptic-scale forcing as described above. The subsequent cessation of high wind speeds in conjunction with rising pressures is also well represented. Wind direction is reasonably captured by the model, although sometimes there is a southerly bias, e.g., between 8 and 10, 25 and 28, and on 4 January. The model shows difficulty simulating the daytime (nighttime) maximum (minimum) near-surface temperature, resulting in a considerable overestimation of its diurnal variation.

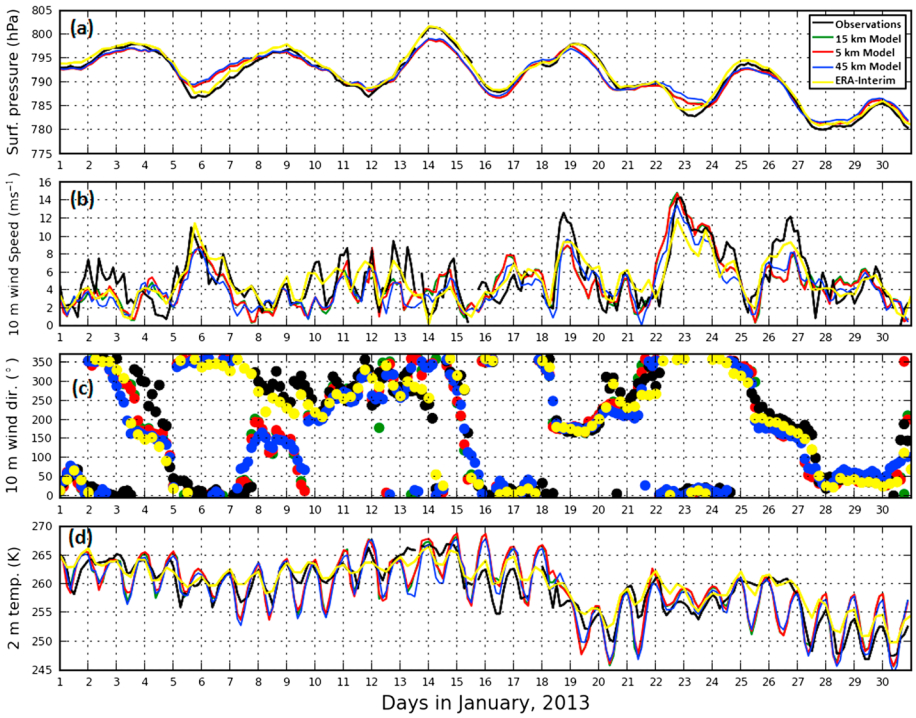

Figure 2. Monthly time series of 3-hourly measurements at Kominko Slade compared with corresponding Polar WRF output from simulations using Run A at 45, 15, and 5 km horizontal resolution for (a) surface pressure (hPa), (b) 10 m wind speed (m s^{-1}), (c) 10 m wind direction (°), and (d) 2 m temperature (K) during January 2013. Also shown are the corresponding time series from ERA-Interim reanalysis data.

This problem is more evident during nighttime than daytime, with the magnitude of the bias varying from a few K to as much as 5–10 K.

Examination of the 3-hourly time series of observations for Kominko Slade during July against the corresponding Polar WRF output from the 5 km resolution domain (Figure 3) suggests that the model skill for surface pressure and 10 m wind speed and direction are largely unchanged compared to January. For example, although the model surface pressure is now generally slightly higher than observed, its temporal variability is again closely captured. Moreover, the model again shows good skill in capturing the rapid strengthening of wind (and warming of near-surface temperature) occurring synchronously with a reduction in surface pressure, e.g., between 19 and 20 July. The small improvement in model skill for wind speed and direction during July compared to January could be partly attributable to the noticeable reduction in variability of the wind speed and direction during July. However, there is a dramatic improvement in model skill for near-surface temperature for July, which perhaps indicates that the model has much less difficulty simulating the relatively slowly changing and small amplitude temperature variability which characterize July. Furthermore, the underestimation of near-surface temperature between 13 and 15 July (by ~10 K) is most likely caused by the easterly bias in the model wind direction during this period, resulting erroneously in the advection of cold continental air rather than relatively warmer northerlies of maritime origin.

Figures 2 and 3 also show the corresponding time series at Kominko Slade from the Polar WRF domains with horizontal grid spacing of 45 and 15 km, as well as from the ERA-Interim reanalysis data. Polar WRF output at horizontal resolutions of 45 and 15 km showed little differences from the 5 km resolution results for both January and July. With the exception of 2 m temperature, ERA-Interim also shows little differences from the model simulations. With regard to 2 m temperature, ERA-Interim often showed a nocturnal warm bias.

Examination of analogous plots for Byrd (not shown) demonstrates that Polar WRF yielded broadly similar results for surface pressure, 2 m temperature, and 10 m wind speed and direction at this site compared to Kominko Slade. In addition, the correlation, bias, and RMSE for Kominko Slade and Byrd (listed in Tables 4 and 5) are also broadly comparable. Surface pressure is represented at both stations with high correlations

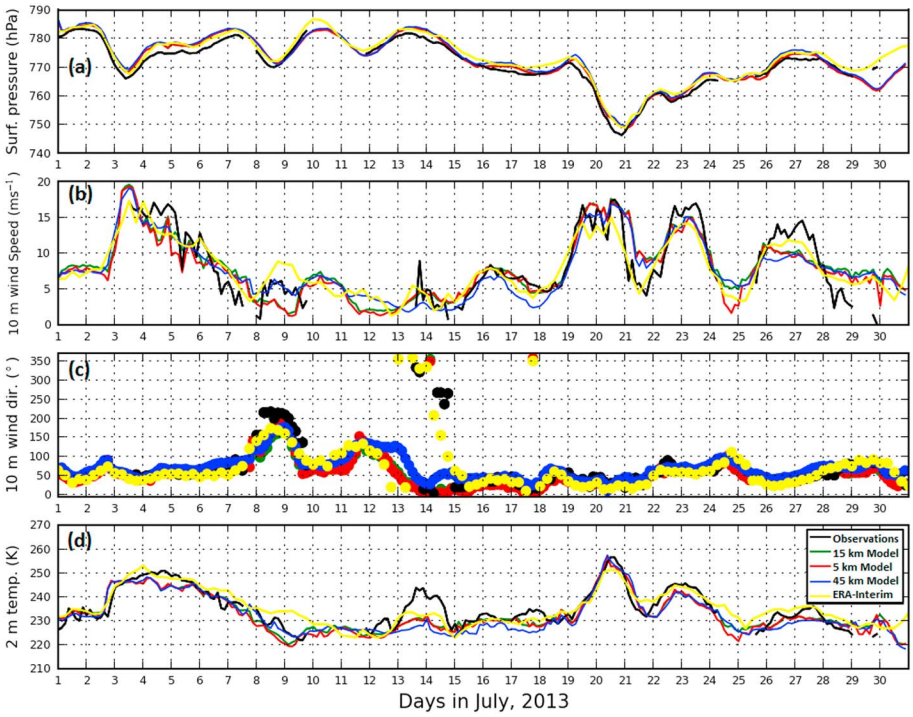

Figure 3. As Figure 2, but for July 2013.

(>0.97). Biases of surface pressure are mostly slightly positive (about 1–3 hPa). The exception to this is at Kominko Slade in January which shows a small bias (−0.06 hPa) due to errors canceling out. At both stations surface pressure RMSE is larger in July (2–4 hPa) than in January (1–2 hPa). The 10 m wind speed correlations are high at both stations (about 0.7–0.8). Biases of 10 m wind speed are mostly slightly negative (around $-1\,m\,s^{-1}$). At both stations the 10 m wind speed RMSE is slightly larger in July (about $3\,m\,s^{-1}$) compared to January (about $2\,m\,s^{-1}$). However, care should be taken in interpreting the wind speed statistics for Byrd in particular due to the large gaps in measurements. The 2 m temperature correlations are above 0.79 at both stations. The biases show a strong seasonal dependence, ranging in magnitude from <0.7 K in January when the diurnal cycle is pronounced (due to positive and negative biases canceling each other out) to about −2 K in July. At both stations the 2 m temperature RMSE is slightly larger in July (about 5 K) compared to January (about 3 K).

3.2. Coastal Stations

Figure 4 compares the monthly 3-hourly time series of observations at Bear Peninsula during January against the corresponding Polar WRF output at a horizontal resolution of 5 km. Some aspects of model performance at Bear Peninsula during January are broadly similar to the inland station Kominko Slade, for example, (1) the temporal variability of both surface pressure and 10 m wind speed are closely captured, (2) a broadly reasonable representation of wind direction with on occasion a southerly bias (e.g., between 6 and 8 and 22 and 25 January), and (3) an exaggerated diurnal cycle in 2 m temperature which is primarily due to difficulty simulating

Table 4. Correlation Coefficient, Bias, and RMSE for Surface Pressure, 10 m Wind Speed and 2 m Temperature for the Polar WRF Simulation Using Run A at the Four AWS Sites for January 2013[a]

	Surface Pressure			10 m Wind Speed			2 m Temperature		
Stations	Correlation	Bias (hPa)	RMSE (hPa)	Correlation	Bias ($m\,s^{-1}$)	RMSE ($m\,s^{-1}$)	Correlation	Bias (K)	RMSE (K)
Kominko Slade	0.98	−0.06	1.25	0.73	−0.59	2.17	0.81	0.01	3.08
Byrd	0.97	1.38	1.98	0.8	−1.24	2.32	0.79	0.69	3.12
Bears Peninsula	0.98	14.31	14.4	0.51	0.83	4.92	0.53	−0.41	3.05
Evans Knoll	0.97	−1.23	1.99	0.33	−0.49	3.33	0.57	−1.59	3.54

[a]The Polar WRF output is at a horizontal resolution of 5 km.

Table 5. Same as Table 4 but for July 2013

	Surface Pressure			10 m Wind Speed			2 m Temperature		
Stations	Correlation	Bias (hPa)	RMSE (hPa)	Correlation	Bias ($m\,s^{-1}$)	RMSE ($m\,s^{-1}$)	Correlation	Bias (K)	RMSE (K)
Kominko Slade	0.98	1.11	2.05	0.84	−0.08	2.61	0.87	−2.01	4.46
Byrd	0.97	2.7	3.6	0.71	−1.46	3.43	0.79	−2.25	5.66
Bears Peninsula	0.97	15.24	15.56	0.59	3.66	8.66	0.79	−2.81	4.81
Evans Knoll	0.98	−1.86	3.04	0.53	−1.15	5.08	0.87	−4.54	7.21

the nighttime minimum near-surface temperature. Notwithstanding these similarities, some notable aspects of model performance specific to Bear Peninsula are as follows: (1) a persistent high pressure bias ranging from around 10 to 15 hPa and (2) difficulty simulating relatively frequent and abrupt changes in wind direction (e.g., between 10 and 16 and 28 and 30 January). Moreover, the model has an improved representation of peak wind speed at Bear Peninsula compared to Kominko Slade. A notable exception to this is the significant overestimation of wind speed by 10–20 $m\,s^{-1}$ between 27 and 30 January, which coincides with an extremely low measured surface pressure of ~925 hPa, suggesting that the cause of this could be related to difficulty in simulating the effects of a deep synoptic weather system. Note that the large positive pressure bias at Bear Peninsula is most likely the result of instrumental error (see section 4 for further discussion).

Examination of the 3-hourly time series of observations for Bear Peninsula during July against the corresponding Polar WRF output from the 5 km resolution domain (Figure 5) suggests that the model skill for surface pressure and 10 m wind speed and direction are largely unchanged compared to January. However, there is an improvement in the representation of 2 m temperature compared to January, despite being systematically underestimated (i.e., the same seasonal dependence found at Kominko Slade). Of particular note is the sustained overestimation of peak wind speed by 5–15 $m\,s^{-1}$ between 4 and 13 July.

Figures 4 and 5 also show the corresponding time series at Bear Peninsula from the Polar WRF domains with horizontal grid spacing of 45 and 15 km, as well as from the ERA-Interim data. While the Polar WRF output at a

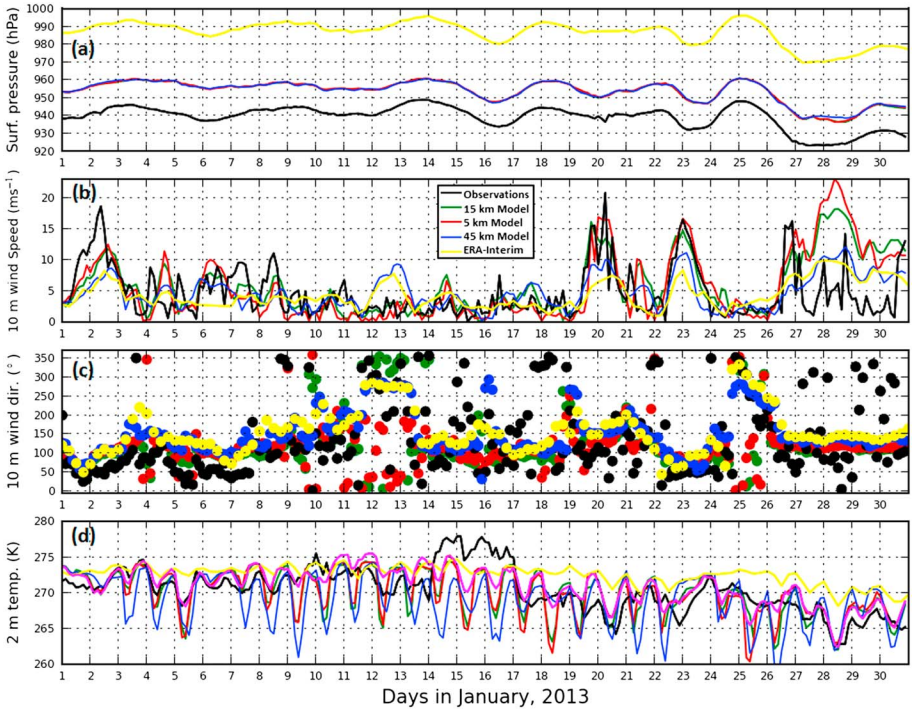

Figure 4. As Figure 2, but for Bear Peninsula during January 2013. (d) The 2 m temperature (magenta line) from the sensitivity experiment Run A1 (which uses the Mellor-Yamada-Janjic boundary layer scheme) at 5 km horizontal resolution.

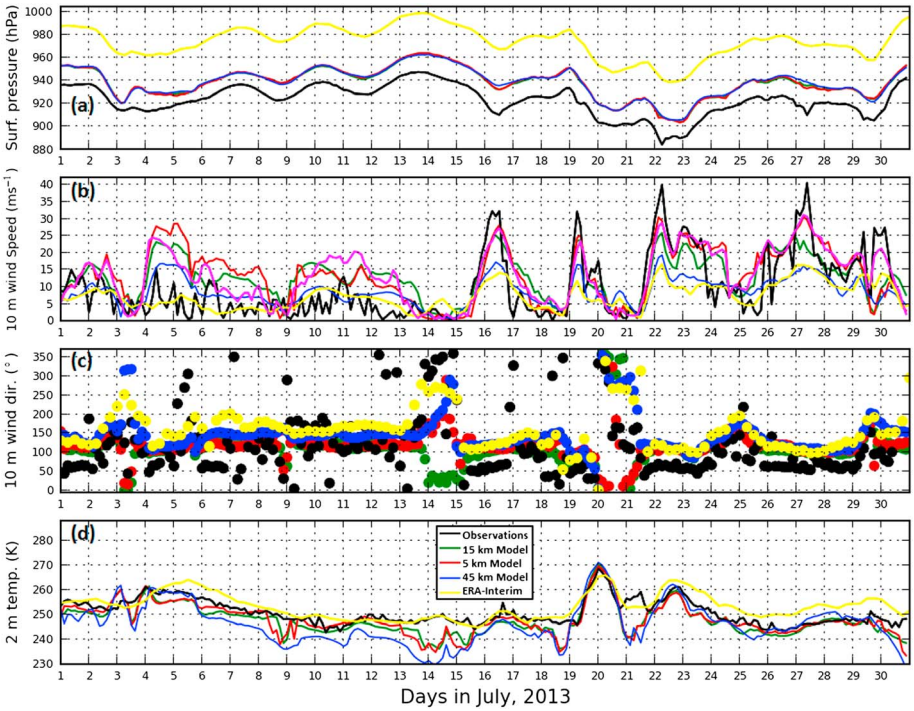

Figure 5. As Figure 2, but for Bear Peninsula during July 2013. (b) The 10 m wind speed (magenta line) from the sensitivity experiment Run D (which uses spectral nudging) at 5 km horizontal resolution.

horizontal resolution of 15 km showed little differences from the 5 km resolution results for both January and July, output from the 45 km resolution differed considerably. Polar WRF output at 45 km resolution showed a large nocturnal cold bias in January and a systematic underestimation of the 10 m wind speed (in particular, the peak wind speeds) for both January and July. Compared to the output at 45 km resolution, ERA-Interim reanalysis data show an even larger underestimation of the 10 m wind speed for both January and July. Additionally, ERA-Interim completely misrepresents the diurnal cycle in 2 m temperature for January but shows a reasonable representation of its temporal variation in July.

The localized wind at coastal sites such as Bear Peninsula is particularly influenced by frequent transient low-pressure systems in the Amundsen Sea. Figures 4 and 5 both show numerous instances of the surface pressure at Bear Peninsula falling and then rising afterward, signaling the approach and departure of a system. In particular, these can act to enhance the strong and directionally constant katabatic flows, which are a characteristic feature of West Antarctic winter climate [*Turner et al.*, 2009]. To investigate whether the sustained overestimation of peak wind speed between 4 and 13 July 2013 at Bear Peninsula could be due to a failure to properly represent the influence of these low-pressure systems, Figure 6 compares the mean sea level pressure between ERA-Interim reanalysis data (Figure 6a) and Polar WRF output (Figure 6c) at 0000 UTC 5 July 2013 (i.e., when the model 10 m wind speed of 20–25 m s^{-1} is around a factor of 2 greater than that measured). Also shown is the infrared cloud image at the same time (Figure 6b). The reanalysis data show a low-pressure system to the northeast of Bear Peninsula, with a central pressure of around 965 hPa. The location and structure of this system is consistent with the well-defined frontal cloud band apparent in the infrared satellite image, suggesting that the reanalysis in this instance is able to reliably capture mean sea level pressure, i.e., the observed large-scale circulation. (Similar analysis of all the low-pressure systems which occurred during January and July 2013 showed that ERA-Interim reanalysis consistently captures the location and structure of low-pressure systems (not shown), thus increasing confidence in the suitability of the reanalysis to provide boundary conditions for the model). However, many aspects of this low-pressure system simulated by Polar WRF differ from the reanalysis. For example, although the central pressure of the model simulated system is also around 965 hPa, it is spatially inconsistent with ERA-Interim; its center is considerably larger (extending as far as the coastline). Consequently, the horizontal pressure gradient at Bear Peninsula is considerably stronger in the model than in the reanalysis, resulting in excessively strong

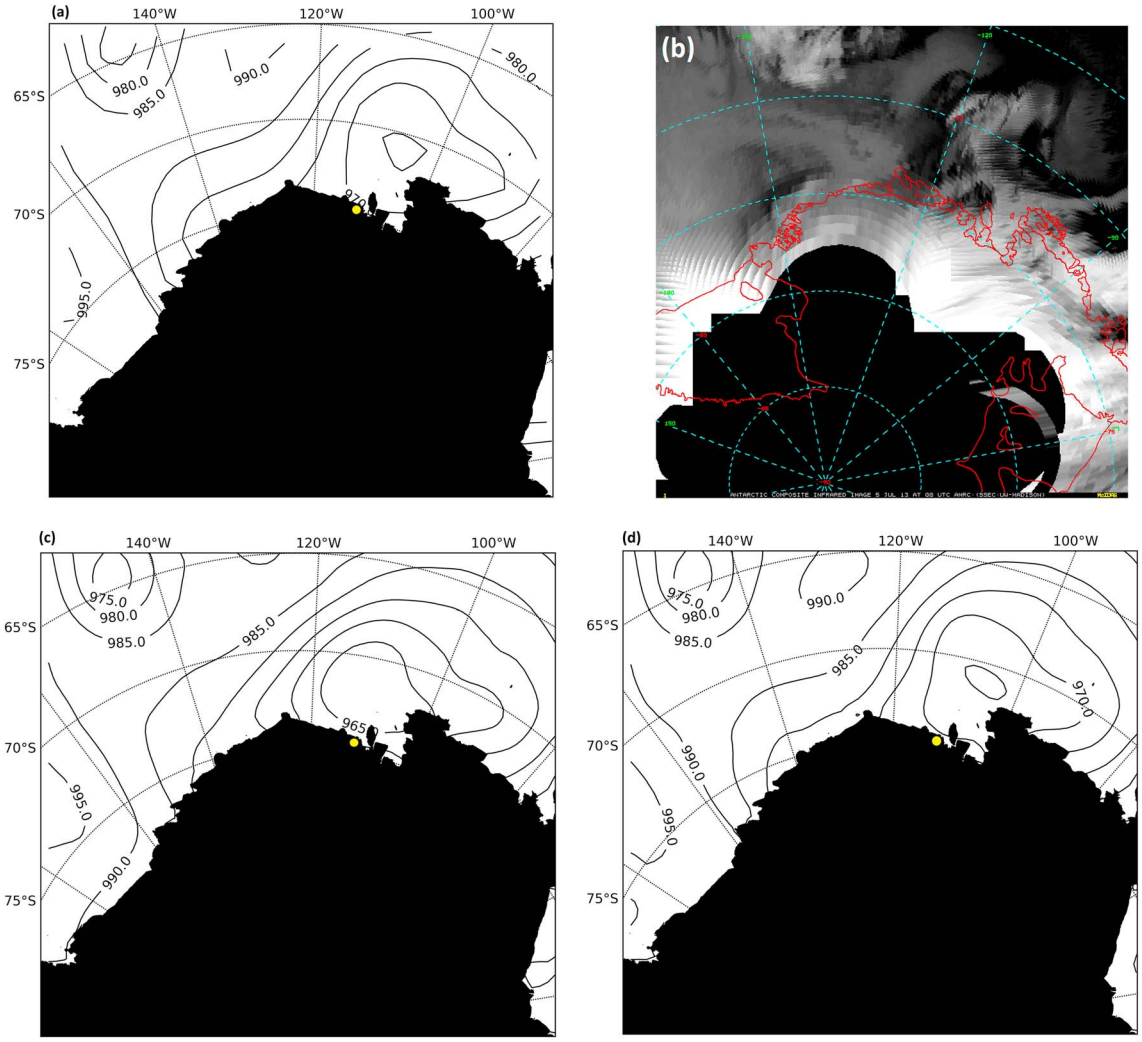

Figure 6. (a) Sea level pressure (hPa, contours) from ERA-Interim reanalysis data and (b) cloud distribution from infrared satellite imagery, both at 0000 UTC, 5 July 2013 over the study domain. Sea level pressure (hPa, contours) from (c) Run A and (d) Run D at a horizontal resolution of 45 km, also at 0000 UTC, 5 July 2013. In Figures 6a, 6c, and 6d the location of Bear Peninsula is shown by a filled yellow circle, while the continent is masked (black). In Figure 6b the red line denotes the coastline, and missing data is masked (black).

winds in the model. By contrast, similar analysis for 0000 UTC 22 July 2013 (i.e., when the measured 10 m wind speed of ~25 m s^{-1} is well captured by the model) showed that the mean sea level field simulated by the model was in good agreement with the reanalysis (not shown). Note that the impact of spectral nudging on model sea level pressure and 10 m wind speed is examined in section 3.3.

Examination of analogous time series plots for Evans Knoll (not shown) demonstrates a mixed model performance relative to Bear Peninsula, which is also apparent from the model statistics (listed in Tables 4 and 5). The most notable improvement at Evans Knoll is the disappearance of the large positive surface pressure bias which exists at Bear Peninsula, i.e., surface pressure biases at Evans Knoll are around −1.5 hPa compared to around 15 hPa at Bear Peninsula. In addition, in July the large positive 10 m wind speed bias at Bear Peninsula (3.66 m s^{-1}) is replaced by a smaller negative bias at Evans Knoll (−1.15 m s^{-1}). However, there is a marked decline in model skill for 10 m wind direction at Evans Knoll compared to Bear Peninsula. The measured wind direction at Evans Knoll is broadly southwesterly, and there is also a notable increase in variability during January compared to July. The model shows a considerable easterly bias in both of these months and a marked failure to represent the high variability in January. Finally, in July there is also a marked increase in the negative 2 m temperature bias and RMSE at Evans Knoll (−4.54 K and 7.21 K, respectively) compared to Bear Peninsula (−2.81 K and 4.81 K, respectively) which could be linked to the easterly wind direction bias.

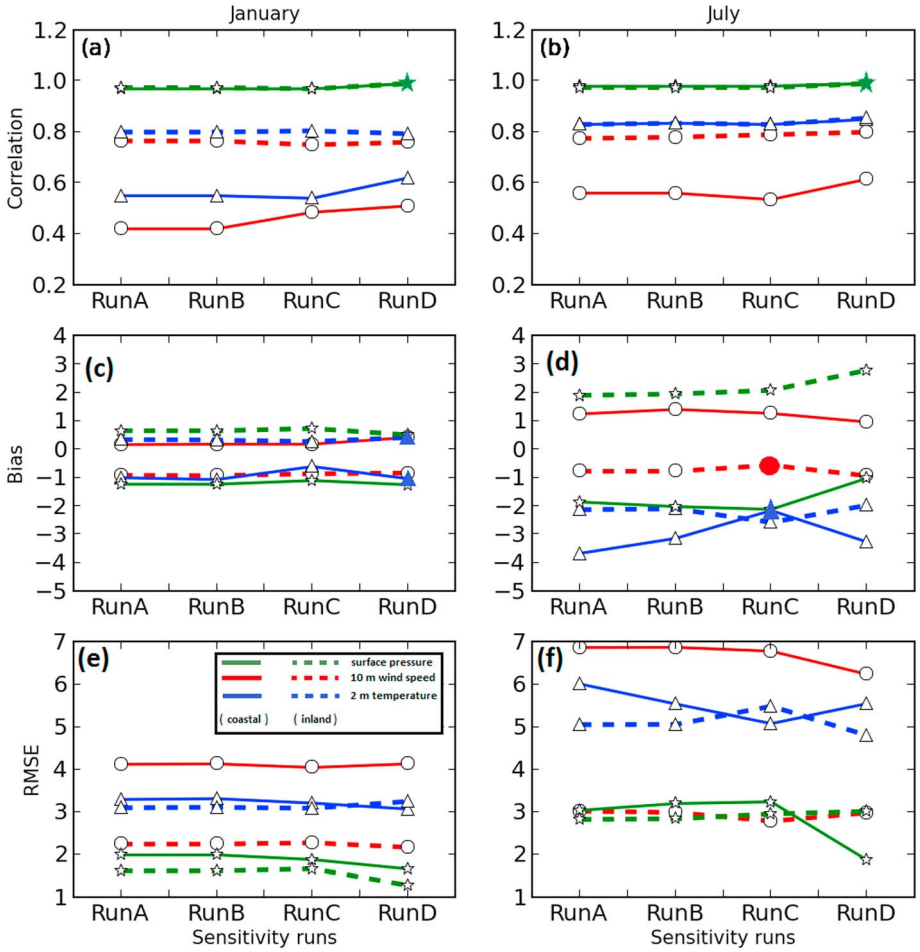

Figure 7. Comparison of the error statistics obtained from the Run A Polar WRF simulations and the three additional sensitivity simulations labeled Run B, Run C, and Run D for surface pressure (green), 10 m wind speed (red), and 2 m temperature (blue) averaged at the coastal (solid line) and inland (dashed line) sites for (a, c, and e) January and (b, d, and f) July 2013. All results are from simulations at a horizontal resolution of 5 km. The statistics are correlation coefficient (Figures 7a and 7b), bias (Figures 7c and 7d), and RMSE (Figures 7e and 7f). Units are same as those used in Table 4. The statistics which are significantly different (at 95% confidence level) are represented by "filled" markers.

The considerable differences between the two coastal stations are consistent with a significant role of localized forcing.

3.3. Sensitivity Experiments

Figure 7 compares model statistics generated from the Run A Polar WRF configuration with corresponding values from the sensitivity simulations labeled Run B, C, and D (listed in Table 3). The statistics are for a horizontal resolution of 5 km and are presented as average values over the two inland and two coastal sites. Note that the surface pressure statistics for the coastal sites are based on results from Evans Knoll only (due to the large surface pressure bias at Bear Peninsula, see Figures 4 and 5). Using realistic high-resolution sea ice and SST data to force the model surface boundary conditions (Run B) or the ~1 km resolution Bedmap2 data set to derive the model orography (Run C) resulted in a reduction in 2 m temperature bias and RMSE for the coastal stations in July (but the reduction in 2 m temperature bias was only significant for Run C). Run C also shows an improvement from ~0.4 to ~0.5 in the correlation coefficient for 10 m wind speed in January over the coastal stations. Note that to gauge the impact of Runs B and C, their statistics should be compared against those for Runs A and B, respectively. To gauge the impact of applying spectral nudging (Run D), the statistics for Run D should be compared to those for Run A. In July, Run D results in substantial improvements at the coastal sites by reducing both the bias and RMSE for surface pressure, 10 m wind speed, and 2 m

Table 6. Comparison of the Error Statistics (Correlation Coefficient, Bias, and RMSE) Obtained From the Run A Polar WRF Simulations and the Two Additional Sensitivity Simulations Labeled Run A1 and A2 for Surface Pressure, 10 m Wind Speed, and 2 m Temperature Averaged at the Coastal and Inland Sites for January 2013[a]

		Correlation Coefficient			Bias			RMSE		
	Variables	Run A	Run A1	Run A2	Run A	Run A1	Run A2	Run A	Run A1	Run A2
Coastal averaged	surface pressure	0.97	0.97	0.97	−1.23	−1.31	−1.37	1.99	2.08	2.09
	10 m wind speed	0.42	0.44	0.43	0.17	0.83	−0.1	4.13	4.28	4.1
	2 m temperature	0.55	0.74	0.52	−1	**−0.06**	−0.59	3.3	2.29	3.08
Inland averaged	surface pressure	0.98	0.97	0.98	0.66	0.63	0.55	1.62	1.66	1.58
	10 m wind speed	0.77	0.76	0.77	−0.92	−0.41	−0.86	2.25	2.17	2.25
	2 m temperature	0.8	0.79	0.78	0.35	1.04	1.05	3.1	3.19	3.3

[a]All results are from simulations at a horizontal resolution of 5 km. Units are the same as those used in Table 4. The statistics which are significantly different (at 95% confidence level) are shown in bold.

temperature, as well as increasing the correlation coefficient for 10 m wind speed. In January, Run D shows an improvement in the correlation coefficients for surface pressure, 10 m wind speed, and 2 m temperature for the coastal sites, as well as a reduction in surface pressure RMSE for both coastal and inland sites. The success of spectral nudging is further evident from Figure 6d, which shows that the application of spectral nudging clearly nudges the model simulated sea level pressure toward ERA-Interim (Figure 6a). Figure 5b additionally shows the 10 m wind speed for Run D at Bear Peninsula during July (see caption for details). This shows that the 10 m wind speed bias was reduced by 5–10 m s^{-1} during much of the first half of July, including the 0000 UTC 5 July 2013 case examined above. Note that equivalent results examining the sensitivity of the model statistics at 15 km horizontal resolution (not shown) were broadly comparable to the 5 km horizontal resolution results.

The model statistics generated from the Run A Polar WRF configuration are compared with the corresponding values from the simulations labeled Run A1 and A2 (which explores the sensitivity to the boundary layer scheme, listed in Table 3) for January (Table 6) and July (Table 7). The statistics are again for a horizontal resolution of 5 km and are presented as average values over the inland and coastal sites. Using the MYJ scheme (Run A1) resulted in a substantial improvement in 2 m temperature at the coastal sites during January by increasing the correlation coefficient and reducing the bias (which is statistically significant) and RMSE. Run A1 also resulted in an improvement in 2 m temperature correlation at the coastal sites during July, but alongside an increase in bias. The success of the MYJ scheme in January is further evident in Figure 4d, which shows that it clearly improves the representation of the diurnal cycle in 2 m temperature (see figure caption for details). The diurnal cycle in 2 m temperature is also improved in January for the inland stations, by often reducing the persistent nocturnal cold bias (not shown). By contrast, the model statistics were largely unchanged using the YSU scheme (Run A2) compared to Run A, i.e., the improvements to 2 m temperature using the MYJ scheme (Run A1) are not apparent.

4. Discussion and Conclusions

This study identified the strengths and weaknesses of Polar WRF (version 3.5.1) simulations of near-surface meteorological variables over West Antarctica in both winter and summer, as well as the sensitivity of the simulations to the choice of a number of different model configurations or boundary conditions. The main strengths of

Table 7. As Table 6 but for July 2013[a]

		Correlation Coefficient			Bias			RMSE		
	Variables	Run A	Run A1	Run A2	Run A	Run A1	Run A2	Run A	Run A1	Run A2
Coastal averaged	surface pressure	0.98	0.98	0.98	−1.86	−1.41	−1.57	3.04	2.63	2.72
	10 m wind speed	0.56	0.61	0.59	1.26	**2.03**	1.32	6.87	6.5	6.73
	2 m temperature	0.83	0.9	0.84	−3.68	−4.6	−2.55	6.01	5.7	5.42
Inland averaged	surface pressure	0.98	0.97	0.97	1.91	1.92	1.95	2.83	2.95	3.03
	10 m wind speed	0.78	0.79	0.75	−0.77	**0.81**	−0.09	3.02	3.09	3.26
	2 m temperature	0.83	0.82	0.82	−2.13	−2.39	−0.8	5.06	5.18	4.99

[a]All results are from simulations at a horizontal resolution of 5 km. Units are the same as those used in Table 4. The statistics which are significantly different (at 95% confidence level) are shown in bold.

the "base" setup (Run A) of the model (which included options such as the MYNN boundary layer scheme, the RRTMG radiation scheme, the WSM5 microphysics scheme, and the Noah land surface model) at a spatial resolution of 5 km are as follows: (1) high skill in simulating pressure at both coastal and inland sites (correlation coefficient $\geq$0.97); (2) wind speed is generally well represented, with improved correlation values at inland sites (0.7–0.8) compared to coastal sites (0.3–0.6); (3) the timing and amplitude of strong wind events are generally well captured at both coastal and inland sites; and (4) good skill for temperature at both coastal and inland sites in winter.

On the other hand, the shortcomings are as follows: (1) on occasion a failure to properly represent transient low-pressure systems and their influence on coastal winds, (2) an amplified diurnal temperature cycle (in particular overly cold nighttime minimum temperatures) in summertime, (3) a general tendency to slightly underestimate the wind speed at the inland sites in summer (bias ranging from -0.6 to $-1.2\,\mathrm{m\,s^{-1}}$), and (4) difficulty representing wind speed and direction when they are rapidly changing.

The above assessment of Polar WRF suggests that the following aspects of the model will require improvements. First, although the model was able to broadly capture the movement and development of cyclonic systems, Polar WRF had difficulty representing mesoscale features of a relatively rapidly evolving system and its response to the complex coastal orography such as around Bear Peninsula in West Antarctica. This had a significantly adverse impact on simulated coastal winds. In Antarctica, the ability of Polar WRF simulations to accurately capture mesoscale features in the evolution of cyclonic systems was previously questioned by *Powers* [2007], while both *Uotila et al*. [2009] and *Nigro et al*. [2012a] found that the ability of Polar WRF to simulate cyclonic systems was reduced near regions of complex coastal orography. Second, the exaggerated diurnal cycle for temperature in the model is a strong indication of problems related to modeled radiative fluxes resulting from difficulties in the simulation of cloud [*Valkonen et al*., 2014]. For example, the pronounced nocturnal cold bias of the model is consistent with a large negative bias in incoming longwave radiation, while the warm model bias in the maximum daytime temperatures is consistent with a positive bias in the incoming shortwave radiation. Such biases in radiative fluxes were found in Polar WRF over the ice shelves to the east of the Antarctic Peninsula by *King et al*. [2015], who noted that they are consistent with the model producing either too little cloud or clouds that are optically thin. Note that temperature biases may also introduce biases in the wind speed, as discussed by *Guo et al*. [2003]. However, biases in wind speed could possibly be reduced by choosing an appropriate value of the surface roughness length for ice. Currently, Polar WRF has a surface roughness length of 1 mm for land ice (which is a factor of two larger than the value measured at Byrd by *Budd et al*. [1964]). Finally, we suspect that the large positive pressure bias at Bear Peninsula is due to the pressure sensor not being calibrated correctly, as possible uncertainty in the measured elevation of the site was ruled out as the cause as this was verified from an independent source.

Improved representation of the boundary layer in Polar WRF also makes a meaningful reduction in temperature [*Valkonen et al*., 2014] and wind speed biases [*Gómez-Navarro et al*., 2015]. This was demonstrated by the sensitivity experiment Run A1 which used the MYJ boundary layer scheme instead of the MYNN scheme, resulting in a much improved representation of the diurnal cycle in 2 m temperature (particularly in January). *Bromwich et al*. [2013b] also found that the MYJ scheme performed better than the MYNN scheme over Antarctica. The sensitivity experiment Run A2 found that the MYJ scheme was also a better choice than the YSU scheme, which was also shown by *Hines and Bromwich* [2008] over Greenland.

The additional sensitivity studies also showed differences in the representation of near-surface meteorological variables over West Antarctica. First the application of spectral nudging resulted in an increase of around 0.1 in the correlation coefficient for wind speed and pressure at the coastal sites during summer, as well as a much improved representation of the mesoscale features of a relatively rapidly evolving cyclonic system and its response to the complex coastal orography of West Antarctica (which additionally benefited the simulation of coastal winds). Comparable investigations of the benefits of spectral nudging on simulating the climate of the Arctic [e.g., *Glisan et al*., 2013; *Berg et al*., 2013] and windstorms in Switzerland [*Gómez-Navarro et al*., 2015] also concluded that simulations using nudging are better than using no nudging. Second, using high-resolution daily satellite sea ice and SST data as surface boundary conditions resulted in an improvement in statistics for temperature at the coastal sites during winter (i.e., a reduction in bias and RMSE by around 1 K), presumably because the sea ice extent in the waters of the Amundsen Sea is particularly extensive during this time of year. However, the statistics showed negligible sensitivity to this change for either the coastal sites during summer (i.e., when the sea ice extent is very much reduced) or at the inland sites during summer and

winter (presumably because the inland sites are primarily affected by winds from the interior). Third, using high-resolution Bedmap2 orography as surface boundary conditions resulted in a relatively small reduction in temperature bias and RMSE during winter, as well as an increase in wind speed correlation during summer, which presumably is attributed to a better representation of the complex coastal orography [*Orr et al*., 2014]. Since the surface elevation at the coastal sites derived from Bedmap2 differ more from the actual elevation compared to GTOPO30 data, the improvements using Bedmap2 are likely due to the better representation of the terrain slope.

Based on these findings, an optimal configuration of Polar WRF with which to run a high-resolution hindcast of West Antarctica climate (which is the long term goal of this work) would include the following: (1) spectral nudging, (2) orography based on the Bedmap2 data set, (3) sea ice boundary conditions from high-resolution daily Bootstrap data (4) SST boundary conditions from high-resolution daily AVHRR data, and (5) MYJ boundary layer scheme in conjunction with Janjic-Eta surface layer scheme.

Regarding the choice of horizontal resolution, our results clearly indicate a strong sensitivity to horizontal resolution at the coastal sites, but not the inland sites. Over the coastal sites the output at 5 and 15 km resolution was largely comparable in skill and considerably more skilful than the output at 45 km resolution or ERA-Interim data. There were even some occasions when the output at 15 km resolution was better than that at 5 km (for example, the wind speed at Bear Peninsula between 28 and 29 January 2013 and between 4 and 9 July 2013 or the wind direction at Bear Peninsula between 14 and 15 July 2013). Given these findings, a recommendation for the horizontal resolution of planned hindcast experiment would be 15 km. Note that this resolution is 3 times higher than current hindcast experiments for Antarctica using WRF and Regional Atmospheric Climate Model, version 2.0 (RACMO2) undertaken as part of the Polar-Coordinated Regional Downscaling Experiment initiative, and a factor of approximately 2 higher than the RACMO2 simulations detailed in *Lenaerts et al*. [2012]. Notwithstanding this, the insensitivity of our results to varying spatial resolution between 5 and 15 km for the coastal region of West Antarctica is at odds when compared to studies such as *Valkonen et al*. [2010], *Elvidge et al*. [2014], *Orr et al*. [2014], and *Gómez-Navarro et al*. [2015]. These studies stressed the need for kilometer-scale grid resolution, which possibly raises doubts as to the quality of the GTOPO30 and Bedmap2 data sets used to make the model orography boundary conditions, i.e., whether they are overly smooth compared to reality. Alternatively, the results could be indicative that the deficiencies in model physics begin to dominate once horizontal resolutions of 5 and 15 km are reached which are able to much better resolve the complex surface forcing which characterizes the coastal margins of West Antarctica. This is in marked contrast to the inland sites, which are characterized by an absence of complex topography resulting broadly in a more homogeneous characterization of its near-surface meteorology and hence largely insensitive to the horizontal resolution examined in this study.

In conclusion, our assessment of the performance of Polar WRF over West Antarctica finds it to be a useful tool for realistically capturing the near-surface meteorological conditions over West Antarctica. However, the systematic biases in temperature and wind fields over parts of West Antarctica are expected to introduce errors in the computation of surface melt pattern [*Trusel et al*., 2013; *Kuipers Munneke et al*., 2014]. These errors will be exacerbated over the coastal region where the temperature already crosses the melting point during summer. Moreover, with surface melt over West Antarctica expected to intensify considerably by the end of the 21st century in response to warming [*Trusel et al*., 2015], projections using Polar WRF could introduce errors in the subsequent simulation of future surface melt patterns over West Antarctica. Our study suggests the need for improvements to Polar WRF physics schemes (e.g., boundary layer) to reduce the temperature and wind biases over Antarctica.

Acknowledgments

The authors appreciate the support of the University of Wisconsin-Madison for the data set, data display, and information from the Automatic Weather Station Program (National Science Foundation (NSF) grant numbers ANT-0944018 and ANT-1245663) and the Antarctic Composite Imagery (NSF grant number ANT-1141908). Special thanks are due to Matthew A. Lazzara (Antarctic Meteorological Research Center, University of Wisconsin-Madison). The study was funded by Natural Environment Research Council (NERC) under grant NEB1115. The authors express their sincere appreciation to David B. Reusch (Department of Earth and Environmental Science, New Mexico Technology), Keith Hines and David Bromwich (Byrd Polar Research Centre, Ohio State University), Kevin Manning (National Center for Atmospheric Research, Boulder, Colorado), and Michiel van den Broeke (University of Utrecht) for useful discussions. The authors would like to thank the three anonymous reviewers for their insightful comments which helped to considerably improve this study.

References

Arrigo, K. R., K. E. Lowry, and G. L. van Dijken (2012), Annual changes in sea ice and phytoplankton in polynyas of the Amundsen Sea, Antarctica, *Deep Sea Res., Part II*, *71*, 5–15, doi:10.1016/j.dsr2.2012.03.006.

Berg, P., R. Döscher, and T. Koenigk (2013), Impacts of using spectral nudging on regional climate model RCA4 simulations of the Arctic, *Geosci. Model Dev.*, *6*, 849–859, doi:10.5194/gmd-6-849-2013.

Bracegirdle, T. J., and G. J. Marshall (2012), The reliability of Antarctic tropospheric pressure and temperature in the latest global reanalyses, *J. Clim.*, *25*, 7138–7146.

Bromwich, D. H., K. M. Hines, and L.-S. Bai (2009), Development and testing of Polar Weather Research and Forecasting model: 2. Arctic Ocean, *J. Geophys. Res.*, *114*, D08122, doi:10.1029/2008JD010300.

Bromwich, D. H., J. P. Nicolas, A. J. Monaghan, M. A. Lazzara, L. M. Keller, G. A. Weidner, and A. B. Wilson (2013a), Central West Antarctica among the most rapidly warming regions on Earth, *Nat. Geosci.*, *6*, 139–145, doi:10.1038/ngeo1671.

Bromwich, D. H., F. O. Otieno, K. M. Hines, K. W. Manning, and E. Shilo (2013b), Comprehensive evaluation of polar weather research and forecasting model performance in the Antarctic, *J. Geophys. Res. Atmos.*, *118*, 274–292, doi:10.1029/2012JD018139.

Budd, W. F., W. R. J. Dingle, and U. Radok (1964), *Studies in Antarctic Meteorology*, *Antarctic Res. Ser.*, 231 pp, vol. 9, AGU, Washington D. C.

Casey, K., T. Brandon, P. Cornillon, and R. Evans (2010), The Past, present, and future of the AVHRR pathfinder SST program, in *Oceanography From Space: Revisited*, edited by V. Barale, J. Gower, and L. Alberotanza, pp. 273–287, Springer, Netherlands, doi:10.1007/978-90-481-8681-5_16.

Chen, F., and J. Dudhia (2001), Coupling an advanced land surface hydrology model with the Penn State NCAR MM5 modeling system. Part I: Model and implementation and sensitivity, *Mon. Weather Rev.*, *129*, 569–585.

Comiso, J. C. (2000), *Bootstrap Sea Ice Concentrations From NIMBUS-7 SMMR and DMSP SMM/I-SSM/S, Version 2, Subset Used: January and July 2013*, NASA DAAC at the National Snow and Ice Data Center, Boulder, Colo.

Condron, A., and I. A. Renfrew (2013), The impact of polar mesoscale storms on northeast Atlantic Ocean circulation, *Nat. Geosci.*, *6*(1), 34–37.

Condron, A., G. R. Bigg, and I. A. Renfrew (2008), Modeling the impact of polar mesocyclones on ocean circulation, *J. Geophys. Res.*, *113*, C10005, doi:10.1029/2007JC004599.

Cuxart, J., et al. (2006), Single-column model intercomparison for a stably stratified atmospheric boundary layer, *Boundary Layer Meteorol.*, *118*, 273–303.

Dee, D. P., et al. (2011), The ERA-Interim reanalysis: configuration and performance of the data assimilation system, *Q. J. R. Meteorol. Soc.*, *137*, 553–597, doi:10.1002/qj.828.

Elvidge, A. D., I. A. Renfrew, J. C. King, A. Orr, and T. A. Lachlan-Cope (2014), Foehn warming distributions in nonlinear and linear flow regimes: a focus on the Antarctic Peninsula, *Q. J. R. Meteorol. Soc.*, doi:10.1002/qj.2489.

Fogt, R. L., and D. H. Bromwich (2008), Atmospheric moisture and cloud cover characteristics forecast by AMPS, *Weather Forecasting*, *23*, 914–930.

Fretwell, P., et al. (2013), Bedmap2: Improved ice bed, surface and thickness datasets for Antarctica, *Cryosphere*, *7*, 375–393, doi:10.5194/tc-6-375-2013.

Giorgi, F., C. Shields Brodeur, and G. T. Bates (1994), Regional climate change scenarios over the United States produced with a nested regional climate model, *J. Clim.*, *7*, 375–399.

Glisan, J. M., W. J. Gutowski Jr., J. J. Cassano, and M. E. Higgins (2013), Effects of spectral nudging in WRF on Arctic temperature and precipitation simulations, *J. Clim.*, *26*, 3985–3999, doi:10.1175/JCLI-D-12-00318.1.

Gómez-Navarro, J. J., C. C. Raible, and S. Dierer (2015), Sensitivity of the WRF model to PBL parametrizations and nesting techniques: Evaluation of surface wind over complex terrain, *Geosci. Model Dev. Discuss.*, *8*, 5437–5479, doi:10.5194/gmdd-8-5437-2015.

Guo, Z., D. H. Bromwich, and J. J. Cassano (2003), Evaluation of Polar MM5 simulations of Antarctic atmospheric circulation, *Mon. Weather Rev.*, *131*(2), 384–411.

Hines, K. M., and D. H. Bromwich (2008), Development and testing of Polar WRF. Part I: Greenland ice sheet meteorology, *Mon. Weather Rev.*, *136*, 1971–1989.

Holtslag, A. A. M., et al. (2013), Stable atmospheric boundary layers and diurnal cycles: Challenges for weather and climate models, *Bull. Am. Meteorol. Soc.*, *94*, 1691–1706.

Hong, S. Y. (2010), A new stable boundary layer mixing scheme and its impact on the simulated East Asian summer monsoon, *Q. J. R. Meteorol. Soc.*, *136*(651), 1481–1496, doi:10.1002/Qj.665.

Hong, S. Y., Y. Noh, and J. Dudhia (2006), A new vertical diffusion package with an explicit treatment of entrainment processes, *Mon. Weather Rev.*, *134*(9), 2318–2341, doi:10.1175/Mwr3199.1.

Hong, S.-Y., J. Dudhia, and S.-H. Chen (2004), A revised approach to ice microphysical processes for the bulk parameterization of clouds and precipitation, *Mon. Weather Rev.*, *132*, 103–120.

Hosking, J. S., A. Orr, G. J. Marshall, J. Turner, and T. Phillips (2013), The influence of the Amundsen-Bellingshausen Seas Low on the climate of West Antarctica and its representation in coupled climate model simulations, *J. Clim.*, *26*, 6633–6648, doi:10.1175/JCLI-D-12-00813.1.

Hunt, J. C. R., A. Orr, J. W. Rottman, and R. Capon (2004), Coriolis effects in mesoscale flows with sharp changes in surface conditions, *Q. J. R. Meteorol. Soc.*, *130*, 2703–2731, doi:10.1256/qj.04.14.

Iacono, M. J., J. S. Delamere, E. J. Mlawer, M. W. Shephard, S. A. Clough, and W. D. Collins (2008), Radiative forcing by long-lived greenhouse gases: Calculations with the AER radiative transfer models, *J. Geophys. Res.*, *113*, D13103, doi:10.1029/2008JD009944.

Irving, D., I. Simmonds, and K. Keay (2010), Mesoscale cyclone activity over the ice-free Southern Ocean: 1999–2008, *J. Clim.*, *23*, 5404–5420, doi:10.1175/2010JCLI3628.1.

Janjić, Z. I. (2002), *Nonsingular Implementation of the Mellor–Yamada Level 2.5 Scheme in the NCEP Meso Model*, *NCEP Off. Note 437*, 61 pp., Natl. Cent. Environ. Predict,, Camp Springs, Md.

King, J. C., J. Turner, G. J. Marshall, W. M. Connolly, and T. A. Lachlan-Cope (2003), Antarctic Peninsula climate variability and its causes as revealed by analysis of instrumental records, in *Antarctic Peninsula Climate Variability: Historical and Paleoenvironmental Perspectives*, *Antarctic Res. Ser.*, vol. 79, edited by E. Domack et al., pp. 17–30, AGU, Washington, D. C.

King, J. C., A. Gadian, A. Kirchgaessner, P. Kuipers Munneke, T. A. Lachlan-Cope, A. Orr, C. Reijmer, M. R. van den Broeke, J. M. van Wessem, and M. Weeks (2015), Validation of the summertime surface energy budget of Larsen C Ice Shelf (Antarctica) as represented in three high-resolution atmospheric models, *J. Geophys. Res. Atmos.*, *120*, 1335–1347, doi:10.1002/2014JD022604.

Kuipers Munneke, P., S. R. M. Ligtenberg, M. R. van den Broeke, and D. G. Vaughan (2014), Firn air depletion as a precursor of Antarctic ice-shelf collapse, *J. Glaciol.*, *60*, 205–214, doi:10.3189/2014JoG13J183.

Lachlan-Cope, T., and W. Connolley (2006), Teleconnections between the tropical Pacific and the Amundsen-Bellingshausen Sea: Role of the El Nino/Southern Oscillation, *J. Geophys. Res.*, *111*, D23101, doi:10.1029/2005JD006386 .

Lenaerts, J. T. M., M. R. van den Broeke, W. J. van deBerg, E. van Meijgaard, and P. Kuipers Munneke (2012), A new, high-resolution surface mass balance map of Antarctica (1979–2010) based on regional atmospheric climate modeling, *Geophys. Res. Lett.*, *39*, L04501, doi:10.1029/2011GL050713.

Liu, P., A. P. Tsimpidi, Y. Hu, B. Stone, A. G. Russell, and A. Nenes (2012), Differences between downscaling with spectral and grid nudging using WRF, *Atmos. Chem. Phys.*, *12*, 3601–3610, doi:10.5194/acp-12-3601-2012.

McMillan, M., A. Shepherd, A. Sundal, K. Briggs, A. Muir, A. Rideout, A. Hogg, and D. Wingham (2014), Increased ice losses from Antarctica detected by CryoSat-2, *Geophys. Res. Lett.*, *41*, 3899–3905, doi:10.1002/2014GL060111.

Medley, B., et al. (2014), Constraining the recent mass balance of Pine Island and Thwaites glaciers, West Antarctica, with airbourne observations of snow accumulation, *Cryosphere*, *8*, 1375–1392, doi:10.5194/tc-8-1375-2014.

Nakanishi, M., and H. Niino (2006), An improved Mellor-Yamada Level-3 model: Its numerical stability and application to a regional prediction of advection fog, *Boundary Layer Meteorol.*, *119*, 397–407.

Nicolas, J. P., and D. H. Bromwich (2011), Climate of West Antarctica and influence of marine air intrusions, *J. Clim.*, *24*, 49–67, doi:10.1175/2010JCLI3522.1.

Nigro, M. A., J. J. Cassano, and S. L. Knuth (2012a), Evaluation of Antarctic Mesoscale Prediction System (AMPS) cyclone forecasts using infrared satellite imagery, *Antarct. Sci.*, *24*, 183–192, doi:10.1017/S0954102011000745.

Nigro, M. A., J. J. Cassano, M. A. Lazzara, and L. M. Keller (2012b), Case study of a barrier wind corner jet off the coast of the Prince Olav Mountains, Antarctica, *Mon. Wea.ther Rev.*, *140*, 2044–2063, doi:10.1175/MWR-D-11-00261.1.

O'Donnell, R., N. Lewis, S. McIntyre, and J. Condon (2011), Improved methods for PCA-based reconstructions: Case study using the Steig et al. (2009) Antarctic Temperature Reconstruction, *J. Clim.*, *24*, 2099–2115, doi:10.1175/2010JCLI3656.1.

Orr, A., J. C. R. Hunt, R. Capon, J. Sommeria, D. Cresswell, and D. Owinoh (2005), Coriolis effects on wind jets and cloudiness along coasts, *Weather*, *60*, 291–299, doi:10.1256/wea.219.04.

Orr, A., T. Phillips, S. Webster, A. Elvidge, M. Weeks, S. J. Hosking, and J. Turner (2014), Met Office Unified Model high resolution simulations of a strong wind event in Antarctica, *Q. J. R. Meteorol. Soc.*, *140*, 2287–2297, doi:10.1002/qj.2296.

Owinoh, A. Z., J. C. R. Hunt, A. Orr, P. Clark, R. Klein, H. J. S. Fernando, and F. T. M. Nieuwstadt (2005), Effects of changing surface heat flux on atmospheric boundary-layer flow over flat terrain, *Boundary Layer Meteorol.*, *116*, 331–361, doi:10.1007/s10546-004-2819-z.

Parish, T. R., and D. H. Bromwich (1998), A case study of Antarctic katabatic wind interaction with large-scale forcing, *Mon. Weather Rev.*, *126*, 199–209.

Powers, J. G. (2007), Numerical prediction of an Antarctic severe wind event with the Weather Research and Forecasting (WRF) model, *Mon. Weather Rev.*, *135*, 3134–3157, doi:10.1175/MWR3459.1.

Powers, J. G., K. W. Manning, D. H. Bromwich, J. J. Cassano, and A. M. Cayette (2012), A decade of Antarctic science support through AMPS, *Bull. Am. Meteorol. Soc.*, *93*, 1699–1712, doi:10.1175/BAMS-D-11-00186.1.

Pritchard, H. D., S. R. M. Ligtenberg, H. A. Fricker, D. G. Vaughan, M. R. van den Broeke, and L. Padman (2012), Antarctic ice-sheet loss driven by basal melting of ice shelves, *Nature*, *484*, 502–505, doi:10.1038/nature10968.

Simmonds, I., K. Keay, and E.-P. Lim (2003), Synoptic activity in the seas around Antarctica, *Mon. Weather Rev.*, *131*, 272–288, doi:10.1175/1520-0493(2003)131<0272:SAITSA>2.0.CO;2.

Skamarock, W. C., J. B. Klemp, J. Dudhia, D. O. Gill, D. M. Barker, M. Duda, X.-Y. Huang, W. Wang, and J. G. Powers (2008), *A Description of the Advanced Research WRF Version 3*, *NCAR Tech. Note, NCAR/TN-475 + STR*, 125 pp., Natl. Cent. for Atmos. Res, Boulder, Colo.

Steig, E. J., D. P. Schneider, S. D. Rutherford, M. E. Mann, J. C. Comiso, and D. T. Shindell (2009), Warming of the Antarctic ice-sheet surface since 1957 International Geophysical Year, *Nature*, *457*, 459–462, doi:10.1038/nature07669.

Steinhoff, D. F., D. H. Bromwich, J. C. Speirs, H. A. McGowan, and A. J. Monaghan (2014), Austral summer foehn winds over the McMurdo dry valleys of Antarctica from Polar WRF, *Q. J. R. Meteorol. Soc.*, *140*, 1825–1837, doi:10.1002/qj.2278.

Sterk, H. A. M., G. J. Steeneveld, and A. A. M. Holtslag (2013), The role of snow-surface coupling, radiation, and turbulent mixing in modelling a stable boundary layer over Arctic sea ice, *J. Geophys. Res. Atmos.*, *118*, 1199–1217, doi:10.1002/jgrd.50158.

Tastula, E. M., T. Vihma, and E. L. Andreas (2012), Evaluation of Polar WRF from modelling the atmospheric boundary layer over Antarctic sea ice in autumn and winter, *Mon. Weather Rev.*, *140*, 3919–3935.

Tastula, E.-M., and T. Vihma (2011), WRF model experiments on the Antarctic atmosphere in winter, *Mon. Weather Rev.*, *139*, 1279–1291, doi:10.1175/2010MWR3478.1.

Thompson, D. W. J., and J. M. Wallace (2001), Annular modes in the extratropical circulation. Part I: Month-to-month variability, *J. Clim.*, *13*, 1000–1016.

Trusel, L. D., K. E. Frey, S. B. Das, P. Kuipers Munneke, and M. R. van den Broeke (2013), Satellite-based estimates of Antarctic surface meltwater fluxes, *Geophys. Res. Lett.*, *40*, 6148–6153, doi:10.1002/2013GL058138.

Trusel, L. D., K. E. Frey, S. B. Das, K. B. Karnauskas, P. Kuipers Munneke, E. van Meijgaard, and M. R. van den Broeke (2015), Divergent trajectories of Antarctic surface melt under two twenty-first-century climate scenarios, *Nat. Geosci.*, doi:10.1038/ngeo2563.

Turner, J., S. N. Chenoli, A. abu Samah, G. Marshall, T. Phillips, and A. Orr (2009), Strong wind events in the Antarctic, *J. Geophys. Res.*, *114*, D18103, doi:10.1029/2008JD011642.

Uotila, P., A. B. Pezza, J. J. Cassano, K. Keay, and A. H. Lynch (2009), A comparison of low pressure system statistics derived from high-resolution NWP output and three reanalysis products over a Southern Ocean, *J. Geophys. Res.*, *114*, doi:10.1029/2008JD011583.

Valkonen, T., T. Vihma, S. Kirkwood, and M. M. Johansson (2010), Fine-scale model simulation of gravity waves generated by Basen nunatak in Antarctica, *Tellus*, *62*, 319–332, doi:10.1111/j.1600-0870.2010.00443.x.

Valkonen, T., T. Vihma, M. M. Johansson, and J. Launiainen (2014), Atmosphere-sea ice interaction in early summer in the Antarctic: Evaluation and challenges of a regional atmospheric model, *Q. J. R. Meteorol. Soc.*, *140*, 1536–1551, doi:10.1002/qj.2237.

van de Berg, W. J., M. R. van den Broeke, C. H. Reijmer, and E. van Meijgaard (2006), Reassessment of the Antarctic surface mass balance using calibrated output of a regional atmospheric climate model, *J. Geophys. Res.*, *111*, D11104, doi:10.1029/2005JD006495.

von Storch, H., H. Langenberg, and F. Feser (2000), A spectral nudging technique for dynamical downscaling purposes, *Mon. Weather Rev.*, *128*, 3664–3673.

Webster, S., M. Uddstrom, H. Oliver, and S. Vosper (2008), A high-resolution modelling case study of a severe weather event over New Zealand, *Atmos. Sci. Lett.*, *9*, 119–128, doi:10.1002/asl.172.

Wilson, A. B., D. H. Bromwich, and K. M. Hines (2012), Evaluation of Polar WRF forecasts on the Arctic System Reanalysis Domain: 2. Atmospheric hydrologic cycle, *J. Geophys. Res.*, *117*, D04107, doi:10.1029/2011JD016765.